Assessment of VCSEL thermal rollover mechanisms from measurements and empirical modeling

Prashant P. Baveja,[1,2,*] **Benjamin Kögel,**[2] **Petter Westbergh,**[2] **Johan S. Gustavsson,**[2] **Åsa Haglund,**[2] **Drew N. Maywar,**[3] **Govind P. Agrawal,**[1] **and Anders Larsson**[2]

[1] *The Institute of Optics, University of Rochester, Rochester, NY, 14627 USA*
[2] *Department of Microtechnology and Nanoscience, Photonics Laboratory, Chalmers University of Technology, Göteborg SE-412 96, Sweden*
[3] *Electrical, Computer and Telecommunications Engineering Technology Dept., Rochester Institute of Technology, Rochester, NY 14623, USA*

[*] *baveja@optics.rochester.edu*

Abstract: We use an empirical model together with experimental measurements for studying mechanisms contributing to thermal rollover in vertical-cavity surface-emitting lasers (VCSELs). The model is based on extraction of the temperature dependence of threshold current, internal quantum efficiency, internal optical loss, series resistance and thermal impedance from measurements of output power, voltage and lasing wavelength as a function of bias current over an ambient temperature range of 15-100°C. We apply the model to an oxide-confined, 850-nm VCSEL, fabricated with a 9-μm inner-aperture diameter and optimized for high-speed operation, and show for this specific device that power dissipation due to linear power dissipation (sum total of optical absorption, carrier thermalization, carrier leakage and spontaneous carrier recombination) exceeds power dissipation across the series resistance (quadratic power dissipation) at any ambient temperature and bias current. We further show that the dominant contributors to self-heating for this particular VCSEL are quadratic power dissipation, internal optical loss, and carrier leakage. A rapid reduction of the internal quantum efficiency at high bias currents (resulting in high temperatures) is identified as being the major cause of thermal rollover. Our method is applicable to any VCSEL and is useful for identifying the mechanisms limiting the thermal performance of the device and to formulate design strategies to ameliorate them.

OCIS codes: (250.7260) Vertical cavity surface emitting lasers; (140.6810) Thermal effects; (200.4650) Optical interconnects; (230.1150) All-optical devices; (060.4510) Optical communications.

References and links

1. W. Hofmann, "High-speed buried tunnel junction vertical-cavity surface-emitting lasers," IEEE Photon. J. **2**, 802–815 (2010).
2. R. Safaisini, J. R. Joseph, and K. L. Lear, "Scalable high-CW-power high-speed 980-nm VCSEL arrays," IEEE J. Quantum Electron. **46**, 1590–1596 (2010).
3. P. Westbergh, J. Gustavsson, Å. Haglund, M. Skold, A. Joel, and A. Larsson, "High speed, low-current-density 850 nm VCSELs," IEEE J. Sel. Top. Quantum Electron. **15**, 694–703 (2009).

#147763 - $15.00 USD Received 23 May 2011; revised 4 Jul 2011; accepted 11 Jul 2011; published 28 Jul 2011

4. J. S. Harris, T. O'Sullivan, T. Sarmiento, M. M. Lee, and S. Vo, "Emerging applications for vertical cavity surface emitting lasers," Semicond. Sci. Technol. **26**, 014010 (2011).
5. B. Ciftcioglu, R. Berman, J. Zhang, Z. Darling, S. Wang, J. Hu, J. Xue, A. Garg, M. Jain, I. Savidis, D. Moore, M. Huang, E. G. Friedman, G. Wicks, and H. Wu, "A 3-D integrated intrachip free-space optical interconnect for many-core chips," IEEE Photon. Technol. Lett. **23**, 164–166 (2011).
6. I. A. Young, E. M. Mohammed, J. T. S. Liao, A. M. Kern, S. Palermo, B. A. Block, M. R. Reshotko, and P. L. D. Chang, "Optical technology for energy efficient I/O in high performance computing," IEEE Commun. Mag. **48**, 184–191 (2010).
7. Y. Ding, W. J. Fan, D. W. Xu, C. Z. Tong, Y. Liu, and L. J. Zha, "Low threshold current density, low resistance oxide-confined VCSEL fabricated by a dielectric-free approach," Appl. Phys. B **98**, 773–778 (2010).
8. Å. Haglund, J. S. Gustavsson, J. Vukušsić, P. Modh, and A. Larsson, "Single fundamental-mode output power exceeding 6 mW from VCSELs with a shallow surface relief," IEEE Photon. Technol. Lett. **16**, 368–370 (2004).
9. C. Ji, J. Wang, D. Söderström, and L. Giovane, "20-Gb/s 850-nm oxide VCSEL operating at 25°C-70°C," IEEE Photon. Technol. Lett. **22**, 670–672 (2010).
10. P. Westbergh, J. S. Gustavsson, B. Kögel, Å. Haglund, and A. Larsson, "Impact of photon lifetime on high speed VCSEL performance," IEEE J. Sel. Top. Quantum Electron. (accepted for publication).
11. A. N. Al-Omari and K. L. Lear, "VCSELs with a self-aligned contact and copper-plated heatsink," IEEE Photon. Technol. Lett. **17**, 1225–1227 (2005).
12. Y. Ou, J. S. Gustavsson, P. Westbergh, Å. Haglund, A. Larsson, and A. Joel, "Impedance characteristics and parasitic speed limitations of high-speed 850-nm VCSELs," IEEE Photon. Technol. Lett. **21**, 1840–1842 (2009).
13. Y.-C. Chang and L. A. Coldren, "Efficient, high-data-rate, tapered oxide-aperture, vertical-cavity surface-emitting lasers," IEEE J. Sel. Top. Quantum Electron. **15**, 1–12 (2009).
14. A. N. Al-Omari and K. L. Lear, "Polyimide-planarized vertical-cavity surface-emitting lasers with 17.0-GHz bandwidth," IEEE Photon. Technol. Lett. **16**, 969–971 (2004).
15. S. B. Healy, E. P. O'Reilly, J. S. Gustavsson, P. Westbergh, Å. Haglund, A. Larsson, and A. Joel, "Active region design for high-speed 850-nm VCSELs," IEEE J. Quantum Electron. **46**, 506–512 (2010).
16. Y. Liu, W.-C. Ng, K. D. Choquette, and K. Hess, "Numerical investigation of self-heating effects of oxide-confined vertical-cavity surface-emitting lasers," IEEE J. Quantum Electron. **41**, 15–25 (2005).
17. P. V. Mena, J. J. Morikuni, S.-M. Kang, A. V. Harton, and K. W. Wyatt, "A simple rate-equation-based thermal VCSEL model," J. Lightwave Technol. **17**, 865–872 (1999).
18. J. W. Scott, R. S. Geels, S. W. Corzine, and L. A. Coldren, "Modeling temperature effects and spatial hole burning to optimize vertical-cavity surface-emitting laser performance," IEEE J. Quantum Electron. **29**, 1295–1308 (1993).
19. G. Hasnain, K. Tai, L. Yang, Y. H. Wang, R. J. Fischer, J. D. Wynn, B. Weir, N. K. Dutta, and A. Y. Cho, "Performance of gain-guided surface emitting lasers with semiconductor distributed bragg reflectors," IEEE J. Quantum Electron. **27**, 1377–1385 (1991).
20. W. Nakwaski and M. Osinski, "On the thermal resistance of vertical-cavity surface-emitting lasers," Opt. Quantum Electron. **29**, 883–892 (1997).
21. P. Debernardi, A. Kroner, F. Rinaldi, and R. Michalzik, "Surface relief versus standard VCSELs: A comparison between experimental and hot-cavity model results," IEEE J. Sel. Top. Quantum Electron. **15**, 828–837 (2009).
22. C. Wilmsen, H. Temkin, and L. Coldren, *Vertical-Cavity Surface-Emitting Lasers: Design, Fabrication, Characterization, and Applications*, (Cambridge Univ. Press, 1999).
23. C. J. Chang-Hasnain, C. E. Zah, G. Hasnain, J. P. Harbison, L. T. Florez, N. G. Stoffel, and T. P. Lee, "Effect of operating electric power on the dynamic behavior of quantum well vertical-cavity surface-emitting lasers," Appl. Phys. Lett. **58**, 1247–1249 (1991).
24. W. H. Knox, D. S. Chemla, G. Livescu, J. E. Cunningham, and J. E. Henry, "Femtosecond carrier thermalization in dense fermi seas," Phys. Rev. Lett. **61**, 1290–1293 (1988).
25. L. A. Coldren and S. W. Corzine, *Diode Lasers and Photonic Intergrated Circuits* (Wiley, 1995).
26. Y.-A. Chang, J.-R. Chen, H.-C. Kuo, Y.-K. Kuo, and S.-C. Wang, "Theoretical and experimental analysis on InAlGaAs/AlGaAs active region of 850-nm vertical-cavity surface-emitting lasers," J. Lightwave Technol. **24**, 536–543 (2006).
27. I. Vurgaftman, J. R. Meyer, and L.-R. Ram-Mohan, "Band parameters for III-V compound semiconductors and their alloys," Appl. Phys. Rev. **89**, 5815–5875 (2001).
28. D. V. Kuksenkov, H. Temkin, and S. Swirhun, "Measurement of internal quantum efficiency and losses in vertical cavity surface emitting lasers," Appl. Phys. Lett. **66**, 1720–1722 (1995).
29. G. R. Hadley, "Effective index model for vertical-cavity surface-emitting lasers," Opt. Lett. **20**, 1483–1485 (1995).
30. A. Larsson, P. Westbergh, J. Gustavsson, Å. Haglund, and B. Kögel, "High-speed VCSELs for short reach communication," Semicond. Sci. Technol. **26**, 014017 (2011).
31. L. F. Lester, S. S. O'Keefe, W. J. Schaff, and L. F. Eastman, "Multiquantum well strained-layer lasers with improved low frequency response and very low damping," Electron. Lett. **28**, 383–385 (1992).
32. K. L. Lear and R. P. Schneider, Jr., "Uniparabolic mirror grading for vertical cavity surface emitting lasers," Appl.

#147763 - $15.00 USD Received 23 May 2011; revised 4 Jul 2011; accepted 11 Jul 2011; published 28 Jul 2011

Phys. Lett. **68**, 605–607 (1996).
33. Y.-A. Chang, T.-S. Ko, J.-R. Chen, F.-I Lai, C.-L. Yu, I.-T. Wu, H.-C. Kuo, Y.-K. Kuo, L.-W. Laih, L.-H. Laih, T.-C. Lu, and S.-C. Wang, "The carrier blocking effect on 850 nm InAlGaAs/AlGaAs vertical-cavity surface-emitting lasers," Semicond. Sci. Technol. **21**, 1488–1494 (2006).

1. Introduction

Vertical-cavity surface-emitting lasers (VCSELs) are key components for communication and sensing applications due to their ease of fabrication and testing, low-power consumption, high beam quality, and high modulation speeds [1–3]. In particular, VCSELs operating in the 850-nm wavelength band constitute an important class of VCSELs. This can be attributed to the availability of commercial multimode fibers that employ VCSELs operating near 850 nm for short-haul communication links in data centers and high-performance computing systems. Further, such VCSELs have shown the potential to play an important role in future high speed optical interconnects and consumer electronics [3–6].

Current-induced self-heating of VCSELs has been identified as a major factor limiting their static [7, 8] and dynamic performance [3, 9, 10]. Self-heating manifests itself as the premature saturation of the output power with increasing bias current, under continuous-wave (CW) operation. Subsequent saturation of the photon density in the active region limits VCSEL's modulation speed. The phenomena responsible for self-heating have received a great deal of attention, both experimentally [11–15] and theoretically [15–21]. Experimental studies on improving the thermally-limited dynamic performance have focused on reducing resistance [3, 12, 14], internal optical absorption [10] and thermal impedance [11]. Theoretical modeling of self-heating effects is a complex problem and involves taking into account various optical, electrical and thermal interactions for the specific VCSEL design under consideration [16, 20, 21].

Previously used thermal models either address the electrical aspects of self-heating effects through an equivalent electrical circuit [17] or employ a detailed physical model by incorporating spatial hole burning, carrier diffusion, and surface recombination [18]. Combined with the laser rate equations, the electrical circuit approach can predict dynamic VCSEL characteristics with appreciable accuracy. However, it uses higher-order polynomials to describe the V-I characteristics, and multiple measurements are required to extract values of all parameters associated with such a model. Moreover, it provides little insight into VCSEL design optimization for improving thermal performance. The model of Scott et al. is important from the standpoint of physical understanding as it incorporates microscopic details of various relevant processes [18]. However, it requires the knowledge of a large number of parameters whose values may not precisely be known for a specific VCSEL, and it also needs to be modified depending on the current injection mechanism. There is, therefore, a need for a generic empirical model which, when coupled with data from basic measurements, can identify major heat sources and quantify their contributions to the total heat load and also relate them to the VCSEL design parameters. Such a model will be useful not only for predicting thermal performance of a VCSEL, but also for providing design guidelines capable of enhancing the thermally-limited device performance.

In this paper, we develop an empirical model to study self-heating effects in VCSELs. The model incorporates the temperature dependence of different macroscopic VCSEL parameters (such as series resistance, threshold current, thermal impedance, internal optical loss, and internal quantum efficiency). We extract this temperature dependence from measurements of output optical power P_{opt}, bias voltage V_b, and emission wavelength λ of the fundamental mode as a function of bias current I_b over an ambient temperature range of 15-100°C and calculate various contributions to self-heating responsible for an increase in the device temperature. The parameters are extracted by performing reliable single-parameter numerical fits to the measure-

#147763 - $15.00 USD Received 23 May 2011; revised 4 Jul 2011; accepted 11 Jul 2011; published 28 Jul 2011

ments. We apply this model to an oxide-confined 850-nm VCSEL, fabricated with a 9-μm inner-aperture diameter and optimized for high speed operation. At room temperature (25°C), as the bias current is increased from threshold to thermal rollover, the saturation of the output power is caused by a 70°C rise in the internal device temperature, which causes the threshold current and internal optical loss to increase by 85% and 43%, respectively, and the internal quantum efficiency to decrease by 20%. Further, for this particular device, at any ambient temperature and bias current, linear power dissipation exceeds the quadratic power dissipation. In addition to quadratic power dissipation, internal optical loss and carrier leakage are the main factors limiting the thermal performance. Our method can potentially be applied to any VCSEL design to pin-point the factors limiting the thermal performance and assess the impact of steps taken to ameliorate them.

The remainder of the paper is organized as follows. In Section 2, we present the theoretical model and outline the method used to extract the temperature dependence of the basic VCSEL parameters. In Section 3, we briefly describe the device under test and the experimental setup. We then present results from measurements over a range of 15-100°C and the extracted temperature dependence of the VCSEL parameters. The simulation results and their comparison with measured data are presented in Section 4. The analysis of thermal rollover mechanisms is presented in Section 5, and the results are summarized in Section 6.

2. Theoretical Model

2.1. Modeling Thermal Effects

There are several mechanisms by which power is dissipated inside a VCSEL [21, 22]. The power dissipated across its series resistance R_s causes resistive or Joule heating. We refer to this mechanism as quadratic power dissipation (QPD), as its dependence on bias current is quadratic, and include it in our model using

$$P_\mathrm{QPD} = R_\mathrm{s}(T_a, I_b) I_b^2. \tag{1}$$

where I_b is the bias current and T_a is the ambient temperature. We have included a direct dependence of series resistance on current caused by charge accumulation at the hetero-interfaces in the distributed Bragg reflectors (DBRs); it leads to a reduction in resistance with bias current [19, 23].

Other sources of power dissipation, including carrier leakage, carrier thermalization, spontaneous carrier recombination, and internal optical loss linearly depend on I_b, both below and above the threshold. We refer to the the sum of these mechanisms as linear power dissipation (LPD) and include it through

$$P_\mathrm{LPD} = K(T) I_b. \tag{2}$$

where $K(T)$ is the LPD coefficient whose value also depends on the device temperature, and therefore on both ambient temperature and current. In these equations, $T = T_a + \Delta T$ is the sum of the ambient temperature T_a and the increase in temperature ΔT caused by bias current induced self-heating. Henceforth, we define the value of a particular device parameter at a fixed T_a and I_b unless specified otherwise.

To model P_LPD, it is important to understand the physical process behind each of the constituent LPD mechanisms. Figure 1 schematically depicts the capture and leakage of carriers injected into the active region of a VCSEL. Our model assumes that a fraction η_i (the internal quantum efficiency) of charge carriers carried by the bias current I_b is captured by the quantum wells; remaining carriers, which constitute carrier leakage, recombine in the barriers and the

#147763 - $15.00 USD Received 23 May 2011; revised 4 Jul 2011; accepted 11 Jul 2011; published 28 Jul 2011

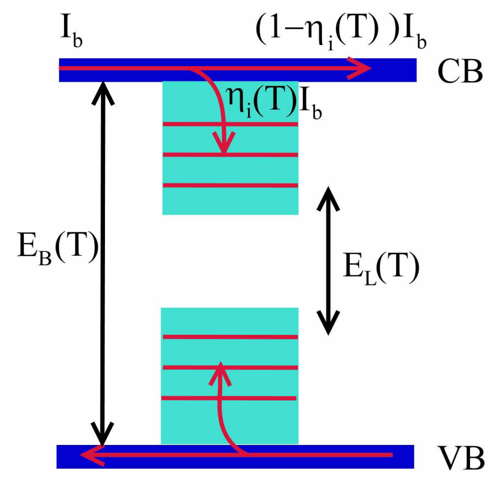

Fig. 1. Schematic illustration of the capture [$\eta_{\mathrm{i}}(T)I_b$] and leakage [(1-$\eta_{\mathrm{i}}(T)I_b$] of injected carriers in strained InGaAs quantum wells. $E_{\mathrm{B}}(T)$, $E_{\mathrm{L}}(T)$ and $\eta_{\mathrm{i}}(T)$ are the temperature-dependent barrier bandgap energy, lasing bandgap energy and internal quantum efficiency, respectively. This figure depicts three out of the four LPD mechanisms; absorption losses in the top and the bottom DBRs are not shown here.

separate-confinement hetero-structure surrounding the quantum wells to generate heat proportional to the dissipated power P_{leak}. Carriers captured by the quantum wells lose energy through various scattering mechanisms [24] (carrier thermalization) and produce the dissipated power P_{therm}. Upon losing energy through thermalization, carriers recombine spontaneously through radiative and non-radiative mechanisms. Since only a small fraction of spontaneously emitted photons couple to the cavity modes, or escape the laser cavity by other means, it is therefore assumed that all spontaneous recombination events produce heat with the dissipated power P_{rec} [25]. Above threshold, a certain fraction of photons generated by stimulated emission are absorbed within the two DBRs forming the VCSEL cavity (internal optical loss). This absorption also produces heat with a dissipated power P_{abs}. Taking all these mechanisms into account, the current dependence of the various power dissipation mechanisms can be written as:

$$P_{\mathrm{leak}} = E_{\mathrm{B}}(T)[1-\eta_{\mathrm{i}}(T)]I_b/q, \tag{3}$$

$$P_{\mathrm{therm}} = [E_{\mathrm{B}}(T)-E_{\mathrm{L}}(T)]\eta_{\mathrm{i}}(T)I_b/q, \tag{4}$$

$$P_{\mathrm{rec}} = \begin{cases} E_{\mathrm{L}}(T)\eta_{\mathrm{i}}(T)I_b/q \quad ; & I_b < I_{\mathrm{th}}, \\ E_L(T)\eta_{\mathrm{i}}(T)I_{\mathrm{th}}(T)/q; & I_b > I_{\mathrm{th}}, \end{cases} \tag{5}$$

$$P_{\mathrm{abs}} = \frac{\eta_{\mathrm{i}}(T)[I_b - I_{\mathrm{th}}(T)][\alpha_{\mathrm{i}}(T)+\alpha_{\mathrm{m}}^{B}(T)]E_{\mathrm{L}}(T)}{q[\alpha_{\mathrm{m}}^{T}(T)+\alpha_{\mathrm{m}}^{B}(T)+\alpha_{\mathrm{i}}(T)]}; \quad I_b > I_{\mathrm{th}}. \tag{6}$$

We assume $P_{\mathrm{abs}} = 0$ for $I_b < I_{\mathrm{th}}$ as not many photons exist inside the VCSEL cavity below threshold. In these equations, $E_{\mathrm{B}}(T)$ and $E_{\mathrm{L}}(T)$ are the temperature-dependent barrier-bandgap energy and laser-photon energy (in eV), respectively, q is the electron charge, I_{th} is the threshold current, $\alpha_{\mathrm{m}}^{T}(T)$ and $\alpha_{\mathrm{m}}^{B}(T)$ are the transmission loss rates through the top and bottom DBRs, respectively, and $\alpha_{\mathrm{i}}(T)$ is the internal optical loss rate. Equation (5) takes into account clamping of the spontaneous recombination rate at the lasing threshold, and Eq. (6) assumes that light emitted through the bottom DBR is also absorbed and therefore produces heat. Note the

#147763 - $15.00 USD Received 23 May 2011; revised 4 Jul 2011; accepted 11 Jul 2011; published 28 Jul 2011

temperature dependence, and consequently the bias current dependence, of most parameters in Eqs. (3)–(6).

When AlGaAs is used as the barrier material in 850 nm VCSELs, the temperature dependence of the barrier bandgap $E_{\mathrm{B}}(T)$ is determined from the Varshini equations [26, 27] for the temperature dependence of the direct bandgap of AlAs and GaAs:

$$E_g(\mathrm{AlAs}) = 3.099 - \frac{0.885\times10^{-3}T_{\mathrm{k}}^2}{T_{\mathrm{k}}+530}, \quad E_{\mathrm{g}}(\mathrm{GaAs}) = 1.519 - \frac{0.5405\times10^{-3}T_{\mathrm{k}}^2}{T_{\mathrm{k}}+204}. \tag{7}$$

where T_{k} is the device temperature in Kelvin. The interpolation formula for the barrier bandgap of $\mathrm{Al}_x\mathrm{Ga}_{1-x}\mathrm{As}$ is known to be [27]:

$$E_g^x(\mathrm{Al_xGa_{1-x}As}) = xE_g(\mathrm{AlAs}) + (1-x)E_g(\mathrm{GaAs}) - x(1-x)(-0.127+1.310x). \tag{8}$$

Temperature dependence of the photon energy E_{L} is estimated from temperature dependence of the lasing wavelength of the fundamental LP_{01} mode.

Above lasing threshold, where self-heating becomes significant, the total P_{LPD} can be written as

$$\begin{aligned} P_{\mathrm{LPD}} &= P_{\mathrm{therm}} + P_{\mathrm{rec}} + P_{\mathrm{leak}} + P_{\mathrm{abs}} \\ &= \frac{1}{q}E_B(T)I_b - \frac{1}{q}E_L(T)\eta_i(T)[I_b - I_{\mathrm{th}}(T)]\left[1 - \frac{\alpha_i(T)+\alpha_m^B(T)}{\alpha_i(T)+\alpha_m^T(T)+\alpha_m^B(T)}\right]. \end{aligned} \tag{9}$$

The total dissipated power (P_{tot}) is thus given by

$$P_{\mathrm{tot}} = P_{\mathrm{QPD}} + P_{\mathrm{LPD}} = \frac{dV_b(T,I_b)}{dI_b}I_b^2 + P_{\mathrm{LPD}}, \tag{10}$$

where the series resistance has been replaced by the differential resistance ($R_s = dV_b/dI_b$) at the given bias point and V_b denotes the applied voltage. The device temperature T, is subsequently obtained using the thermal impedance R_{th} which relates the change in device temperature to the dissipated power and can be written as [3, 17]

$$T = T_a + \Delta T = T_a + R_{\mathrm{th}}(T)P_{\mathrm{tot}}. \tag{11}$$

Note that R_{th} also depends on temperature through temperature dependence of the thermal conductivities of various materials in the VCSEL structure [20]. We stress that the series (or differential) resistance in Eq. (1) and the linear power dissipation coefficient in Eq. (2) depend strongly on temperature, and therefore also on the bias current. The consequences of this are strong deviations from quadratic and linear dependencies of P_{QPD} and P_{LPD}, respectively, on the bias current for the VCSELs operating under continuous bias current.

Finally, we calculate the optical power emitted through the top DBR, at a given current and ambient temperature, using [25]:

$$P(T,\, I_b) = \frac{\eta_i(T)[I_b - I_{\mathrm{th}}(T)]\alpha_m^T(T)}{\alpha_m^T(T)+\alpha_m^B(T)+\alpha_i(T)}\left(\frac{hc}{q\lambda(T)}\right). \tag{12}$$

where $\lambda(T)$ is the emission wavelength of the fundamental mode, c is the speed of light and h is the Planck constant.

2.2. *Extraction of parameters from measurements*

In the preceding analysis, we derived the equations used to relate the dissipated power P_{tot}, device temperature T, and output power P_{opt} to the bias current. These equations contain a number of parameters whose temperature dependence needs to be quantified. To achieve this, we measure the output power, voltage and emission wavelength as a function of the bias current over a range of T_a (15-100 °C). The measurements are performed under continuous or low-duty-cycle pulsed operation.

The measurements for extracting the temperature dependence of VCSEL parameters are performed over a range of bias currents close to the lasing threshold. Any bias current-induced increase in temperature, ΔT, depends on the ambient temperature T_a owing to the temperature dependence of thermal impedance [Eq. (11)] and the increasing difficulty faced in stabilizing high stage temperatures against room temperature. At low ambient temperatures ($T_a \leq 50°\text{C}$), the error in the extracted parameter values corresponds to a bias current induced increase in the device temperature ($\Delta T \leq 2°\text{C}$). As discussed in the next section, this corresponds to the resolution limit of the device thermometer [3]. With increasing ambient temperature, ΔT increases. The corresponding errors in the reported parameter values at room temperature ($T_a = 25°\text{C}$) are summarized in Tables 1 and 2, assuming a worst-case value of 5°C uncertainty at $T_a = 100°\text{C}$.

The temperature dependence of the emission wavelength, $\lambda(T)$, is found by measuring the wavelength of the fundamental mode (LP_{01}) as a function of ambient temperature [3]. For GaAs-based 850-nm VCSELs, the value of $\Delta\lambda/\Delta T$ is typically around 0.06 nm/°C. This quantity is also used to estimate the device temperature at various values of T_a and I_b.

The temperature dependence of the threshold current, $I_{\text{th}}(T)$, is extracted from power versus current (P_{opt}–I_b) measurements recorded at different ambient temperatures [3].

The internal optical loss, $\alpha_i(T)$, is extracted from the measured dependence of output power on bias current just above threshold for VCSELs with different top-DBR reflectivities. This reflectivity is varied by changing the thickness of the top layer (using dry etching), which controls the phase of the surface reflection. The method is described in [10]. By performing these measurements at different ambient temperatures, the temperature dependence of $\alpha_i(T)$ is obtained. Other methods for carrying out these measurements for any VCSEL have been previously reported [28].

The temperature dependence of the internal quantum efficiency, $\eta_i(T)$, is also extracted from the measured P_{opt}–I_b curves. The slope efficiency (SE) is extracted from the P_{opt}–I_b curves at different ambient temperatures by averaging the slope dP_{opt}/dI_b over optical powers in the range of P_1 and P_2. The choice of P_1 and P_2 is constrained such that the increase in the device temperature over this range should be negligible ($\Delta T \leq 5°C$). Therefore, P_1 is chosen as emitted power at the lasing threshold at a particular ambient temperature and P_2 is chosen as 10% of the maximum emitted power at room temperature. The external differential quantum efficiency is then calculated using [22, 25]

$$\eta_d(T) = \frac{q\lambda(T)}{hc}\,\text{SE}(T). \tag{13}$$

We then calculate $\eta_i(T)$ using the relation

$$\eta_d(T) = \frac{\eta_i(T)\alpha_m^T(T)}{[\alpha_m^T(T) + \alpha_m^B(T) + \alpha_i(T)]}. \tag{14}$$

Here, the temperature dependence of the transmission loss rates through the top and bottom DBRs is accurately calculated using an effective index model that takes into account the temperature dependence of the refractive index of the constituent layers of the DBRs [10, 29].

#147763 - $15.00 USD Received 23 May 2011; revised 4 Jul 2011; accepted 11 Jul 2011; published 28 Jul 2011

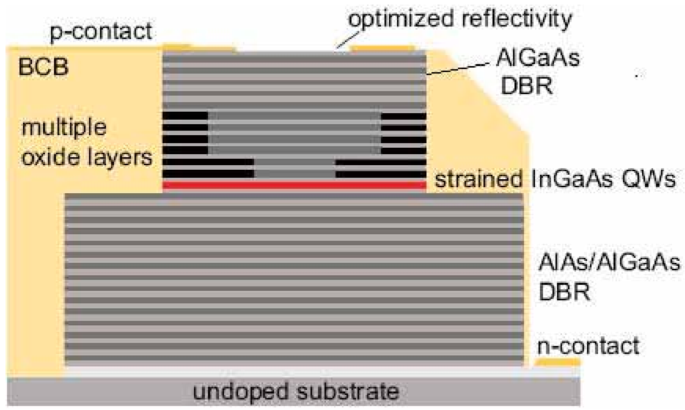

Fig. 2. Schematic cross section of the high-speed 850-nm VCSEL used in the experiment. Benzo-cyclo-butene (BCB) is employed to reduce parasitic capacitance. Six layers are used for forming an oxide aperture (dark shading region). Other details of the device design can be found in Ref. [30].

Finally, temperature dependence of the thermal impedance, $R_{\mathrm{th}}(T)$, is estimated by measuring the change in the emission wavelength, and therefore the increase in the device temperature, with increasing dissipated power in the current range $I_b < 2I_{\mathrm{th}}$ at different ambient temperatures [11, 20]. This is done so that temperature increase due to bias-current induced self-heating is negligible.

3. Measurements on the Device Under Test

3.1. Device Under Test

The structure of the VCSEL used for the experiments is schematically depicted in Fig. 2. Our VCSEL operates at wavelengths near 850-nm. It is grown on a GaAs substrate and employs an oxide-confined configuration optimized for high speed modulation [30]. The top and bottom DBRs are fabricated with graded interfaces and modulation doping to reduce their electrical resistance [3]. The bottom DBR is partly composed of binary (AlAs) material to lower its thermal impedance [10]. The active region is made of five strained InGaAs quantum wells to improve its differential gain [15] and is surrounded by a separate confinement hetero-structure designed for efficient carrier trapping and low gain-compression [30, 31]. As indicated with dark shading in Fig. 2, six AlGaAs layers in the lower part of the top DBR are composed of high Al-content, (98% for the bottom two and and 96% for the remaining four) to form a small oxide aperture (9 μm diameter) for current and optical confinement and a larger oxide aperture (18 μm diameter) for reducing device capacitance [10, 13]. In a second dry-etching process, the bottom contact layer is reached and the n-contact layer is evaporated. The etched mesas are embedded in a low-k dielectric (benzo-cyclo-butene or BCB) to further reduce the parasitic capacitance [1, 3, 12].

3.2. Experimental setup and measurements

For measuring the emitted optical power and voltage as a function of bias current, the VCSEL was placed on a copper stage with active temperature control and stabilization. The light emitted by the VCSEL was detected by a calibrated, large-area photodiode (UDT Sensors PIN-10D) for accurate power measurement. Measurements were performed over an ambient temperature range of 15-100°C. For spectral measurements, the light was coupled to a multimode fiber

#147763 - $15.00 USD Received 23 May 2011; revised 4 Jul 2011; accepted 11 Jul 2011; published 28 Jul 2011

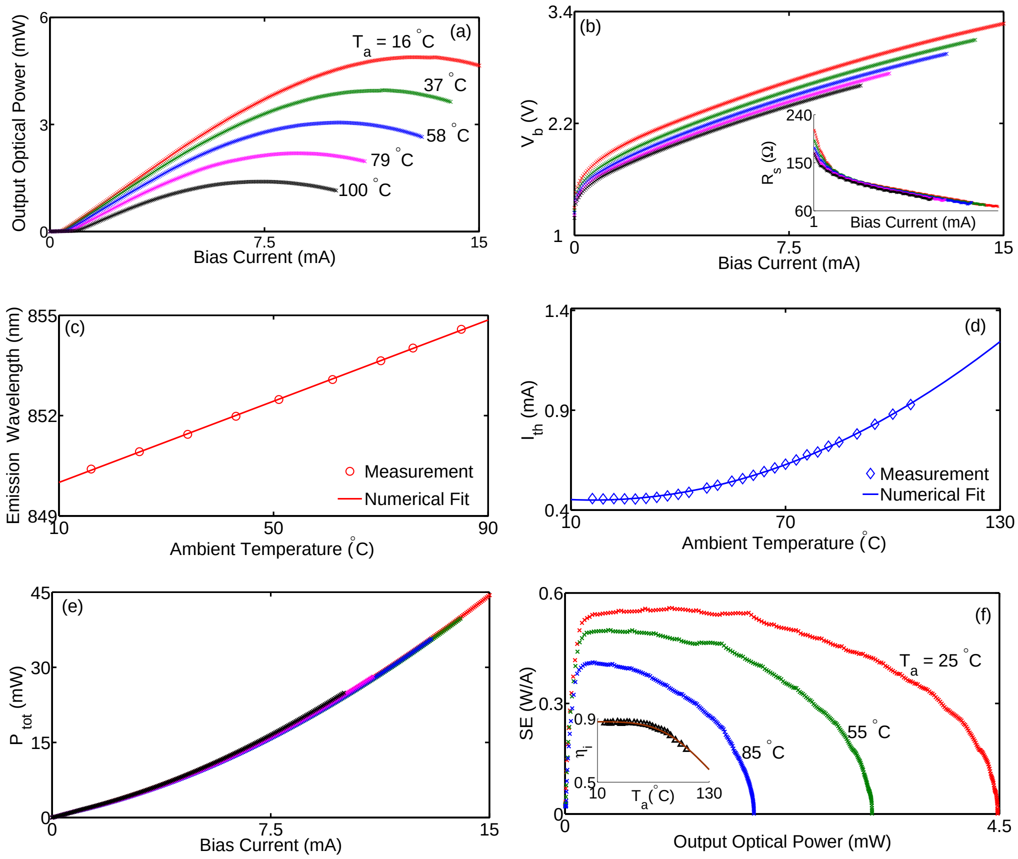

Fig. 3. Measurements used to extract temperature dependence of VCSEL parameters. (a) Output power and (b) voltage as a function I_b at five ambient temperatures. The inset in (b) shows variations of differential resistance R_s with I_b. (c) Wavelength of the (LP_{01}) mode versus T_a (circles); the linear fit is used to estimate the device temperature. (d) Threshold current as a function of T_a; the numerical fit is used in the thermal model. (e) Dissipated power as a function of I_b for five T_a values used in part (a). (f) Slope efficiency versus output power at three different T_a values. The inset shows the derived dependence of η_i on temperature; the numerical fit is used in the thermal model.

connected to an optical spectrum analyzer. All spectral measurements were performed with 0.1 nm resolution. As a result, device temperatures deduced from spectral data are accurate to within 1.6°C.

Experimental data from measurements are presented in parts (a) to (c) of Fig. 3. Part (a) shows the emitted optical power versus bias current I_b under CW operation at different ambient temperatures T_a. Clearly, the slope efficiency decreases and the threshold current I_{th} increases with increasing T_a. The corresponding dependence of voltage V_b on I_b at different T_a is shown in part (b). At a given I_b, V_b decreases with increasing T_a due to a reduction of the bandgap and improved carrier transport through the DBRs at higher temperatures. The inset Fig. shows the dependence of differential resistance (R_s) on I_b at different T_a. It can be seen that R_s decreases much more rapidly with increasing I_b, as opposed to increasing T_a. This can be attributed to an increase in charge accumulation at DBR interfaces with increasing bias current [19, 23]. The dependence of R_s on I_b and T_a is used to calculated P_{QPD} at any combination of current and

#147763 - $15.00 USD Received 23 May 2011; revised 4 Jul 2011; accepted 11 Jul 2011; published 28 Jul 2011

Table 1. Room Temperature Values of VCSEL Parameters

Parameter	Value
λ	850.9 ± 0.31 nm
R_{th}	1.965 ± 0.029°C mW^{-1}
α_i	$(7.0 \pm 0.21) \times 10^{-2}$ ps^{-1}
α_m^T	5.89×10^{-2} ps^{-1}
α_m^B	6.27×10^{-3} ps^{-1}

T_a. Figure 3(c) shows the emission wavelength of the fundamental LP_{01} mode at different T_a, measured close to lasing threshold to avoid self-heating. The deduced linear dependence of wavelength on temperature is subsequently used to find the device temperature at any combination of T_a and I_b under CW operation.

3.3. Extraction of VCSEL Parameters

Plots used for extracting the temperature dependence of various parameters are shown in parts (d) to (f) of Fig. 3. Part (d) shows the dependence of I_{th} on device temperature, with minimum I_{th} occurring at the temperature for which the gain peak is spectrally aligned with the cavity resonance (30°C for the device under test) [22]. Here we use a two-segment line-fit to calculate threshold current at any ambient temperature from the corresponding P_{opt}–I_b curve. This method is relatively insensitive to changes in slope efficiency [25]. A parabolic numerical fit is used to model the dependence of I_{th} on T_a. The maximum error in the calculated value of I_{th} is less than 2% at any T_a. Part (e) shows the dependence of dissipated power, $P_{\mathrm{tot}} = I_b V_b - P_{\mathrm{opt}}$, on I_b at different ambient temperatures. At any bias current, a slight increase in dissipated power with increasing T_a is observed. The reason behind this will be discussed in detail in Section 5. Part (f) shows the dependence of slope efficiency on output power at different T_a. Following the procedure outlined in Section 2.2 and using Eqs. (13) and (14), the dependence of the internal quantum efficiency (η_i) on the device temperature is deduced and plotted in the inset of Fig. 3(f). The η_i is nearly constant and close to 88% at low device temperatures, but it decreases quite rapidly as the device temperature is increased beyond 50°C. A polynomial fit is used to represent $\eta_i(T)$. The maximum calculated error in the extracted value of η_{i} is less than 1 % at any T_a. To enable the calculation of $\eta_i(T)$ from Eq. (14), we use values for the internal optical loss obtained using the method outlined in [10] and briefly described in Section 2. The internal optical loss was found to increase linearly with ambient temperature, from 0.070 ps^{-1} at 25°C, to 0.097 ps^{-1} at 85°C. This is consistent with the linear dependence of the free-carrier absorption coefficient on temperature [10].

Tables 1 and 2 list several device parameters whose value was found to vary linearly with temperature. Table 1 lists the room temperature values, while Table 2 lists the slope of the linear temperature dependence. These tables also summarize the error in the measured values of VCSEL parameters. The origin of this error has been discussed in Section 2.2. Since $\alpha_{\mathrm{m}}^T(T)$ and $\alpha_{\mathrm{m}}^B(T)$ are calculated numerically, their values are assumed to be accurate. Physical explanation behind the temperature dependence as well as previously reported room temperature values for these parameters can be found in [3, 10, 20, 29].

#147763 - $15.00 USD Received 23 May 2011; revised 4 Jul 2011; accepted 11 Jul 2011; published 28 Jul 2011

Table 2. Linear Temperature Dependence of VCSEL Parameters ($\triangle = \frac{\partial}{\partial T}$)

Parameter	Value
$\triangle\lambda$	$(6.07 \pm 0.13) \times 10^{-2}$ nm°C^{-1}
$\triangle R_{th}$	$(5.4 \pm 0.4) \times 10^{-3}$ mW^{-1}
$\triangle\alpha_i$	$(4.167 \pm 0.11) \times 10^{-4}$ ps^{-1}°C^{-1}
$\triangle\alpha_m^T$	-3.622×10^{-5} ps^{-1}°C^{-1}
$\triangle\alpha_m^B$	-5.705×10^{-6} ps^{-1}°C^{-1}

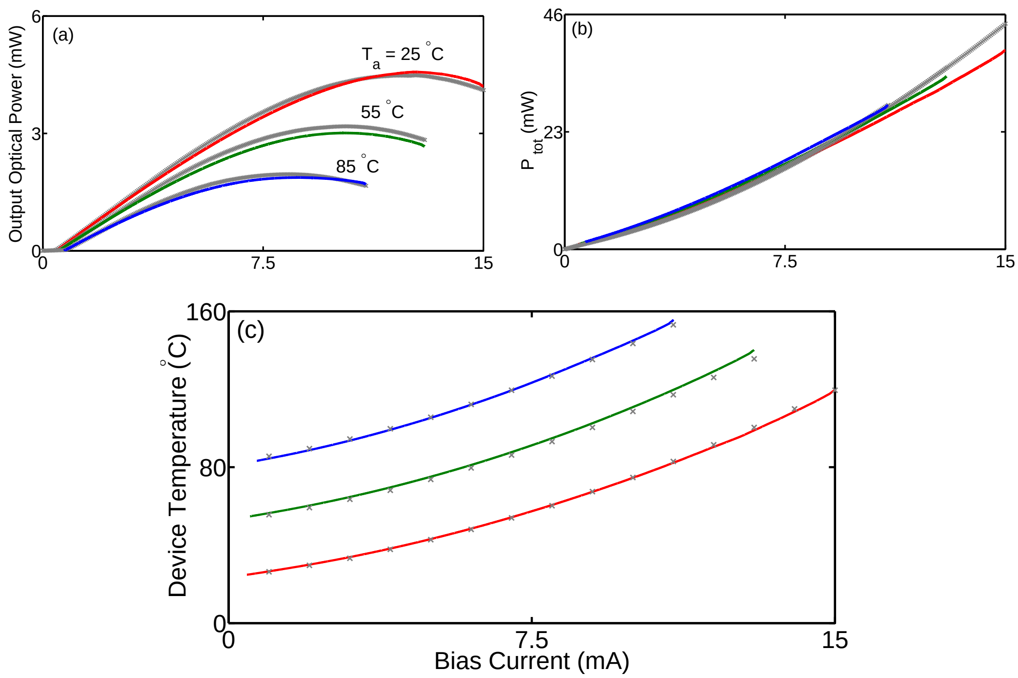

Fig. 4. Comparison of simulated (solid lines) and measured (symbols) values of (a) output power, (b) total dissipated power, and (c) device temperature as a function of I_b at three different ambient temperatures [$T_a = 25$, 55, and 85°C].

4. Predictions from the Thermal Model

After having deduced the temperature dependence of all VCSEL parameters from the experimental data, our empirical thermal model should be able to reproduce measured VCSEL characteristics. We use the procedure outlined in Section 2, with the parameters listed in Tables 1 and 2 to numerically calculate various contributions to the dissipated power. Parts (a) to (c) of Fig. 4 show the measured and simulated output powers, total dissipated powers, and device temperatures as a function of I_b at three ambient temperatures ($T_a = 25$, 55 and 85°C). The theoretical predictions based on Eqs. (10)–(12) are found to be in good agreement with the measured data for all values of I_b. This agreement depicts the optical, electrical, and thermal consistency of our thermal model as well as underlying accuracy of the extracted temperature dependence of various VCSEL parameters.

#147763 - $15.00 USD Received 23 May 2011; revised 4 Jul 2011; accepted 11 Jul 2011; published 28 Jul 2011

To understand the reason behind the saturation of output power at high bias currents, we plot in Fig. 5 the evolution of selected VCSEL parameters with bias current at $T_a = 25$, 55, and 85°C. Part (a) shows variation of η_i with I_b. At 25°C ambient temperature, η_i is reduced from 88% at threshold to 70% at thermal rollover where the device temperature is close to 100°C as shown in Fig. 4(c). The reduction in η_i becomes more severe at higher ambient temperatures. For example, when $T_a = 85$°C, η_i is reduced to less than 50% at thermal rollover. Figure 5(b) shows the evolution of I_th with I_b. As expected, the threshold current increases with bias current because of current-induced self-heating. The inset plots the derivative dI_th/dI_b as a function of I_b and shows that this derivative becomes so large near thermal rollover that the rate of increase of I_th is 0.2 times the change in I_b. Ideally, an I_th insensitive to I_b over a wide range of device temperatures is desired, from the standpoint of improving the device thermal performance. This can be achieved by optimizing wavelength detuning between the gain-peak and the cavity resonance at which the VCSEL operates [1, 22].

The VCSEL thermal saturation behavior can now be explained as follows: at any T_a, as I_b increases, the power dissipated within the VCSEL increases [Eq. (10)]. The corresponding increase in temperature [Eq. (11)] reduces η_i and increases I_th and α_i, which eventually causes the thermal rollover. To delay the onset of thermal rollover, the rate of increase of T with respect to I_b must be reduced. Traditionally, this has been achieved by reducing series resistance R_s [3, 12, 14] and R_th [11, 20]. In this work, however, we focus on identifying and quantifying the relative contributions to linear power dissipation (P_LPD) in our device with an aim to formulate design strategies to reduce them. For this purpose, we plot the LPD coefficient K introduced in Eq. (2). The three curves in Fig. 5(c) show the total K representing the sum of four individual contributions at three ambient temperatures [$T_a = 25$, 55, and 85°C]. As seen there, K initially decreases with increasing I_b, reaches a minimum value, and then starts increasing as I_b approaches the bias current corresponding to thermal rollover. It is this increase of K with current that causes a rapid increase in internal temperature of our VCSEL, which in turn causes the thermal rollover behavior.

To understand the peculiar behavior of $K(I_b)$, we decompose the LPD coefficient into individual coefficients for the four constituent LPD mechanisms. We attach a subscript to K and introduce $K_\mathrm{d} = P_\mathrm{d}/I_b$, where d is the subscript label used in Eqs. (3)–(7) that identifies the specific LPD mechanism in question. Four individual K parameters are calculated from Eqs. (3)–(7) by simply dividing the four equations with I_b. In Fig. 5(d) we plot these individual LPD coefficients as a function of bias current at $T_a = 25$°C. The total K is also plotted for comparison.

The LPD coefficients representing heating due to carrier leakage and thermalization are fairly constant over a large range of I_b but the other two change considerably. Consider first heating due to the carrier recombination governed by K_rec. This parameter is large at low bias currents and decreases as I_b increases. This can be understood by noting that heating due to spontaneous recombination is high below laser threshold as most injected carriers recombine spontaneously to produce heat. It is reduced near and beyond the laser threshold because of a clamping of the carrier density. Consider next heating due to internal optical loss (absorption of photons produced by stimulated emission) governed by K_abs. This heating mechanism starts at laser threshold and its contribution increases with I_b due to an increase in the number of stimulated photons generated inside the laser cavity. The net effect of K_rec and K_abs is an initial reduction of $K(I_b)$ with increasing I_b around threshold.

The region bounded by the two vertical dotted lines in Fig. 5(d) corresponds to the region where total K takes its relatively low values. In this region, the coefficients representing thermalization and absorption heating are nearly constant while the coefficients representing spontaneous recombination and carrier leakage are slowly decreasing and increasing, respectively.

#147763 - $15.00 USD Received 23 May 2011; revised 4 Jul 2011; accepted 11 Jul 2011; published 28 Jul 2011

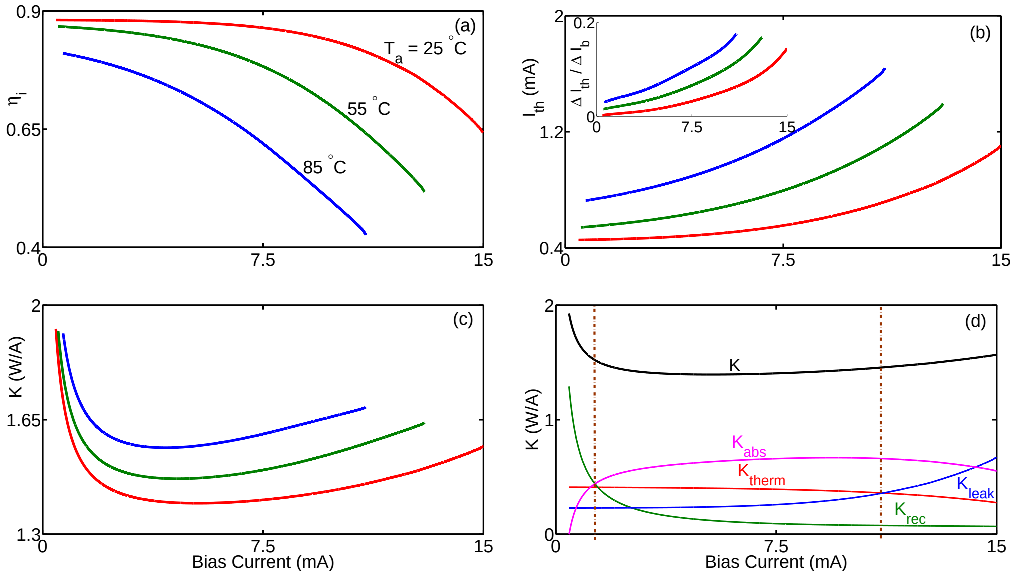

Fig. 5. (a) Internal quantum efficiency, (b) threshold current, and (c) LPD coefficient K versus current at three ambient temperatures. The inset in (b) shows the derivative dI_{th}/dI_b as a function of I_b. (d) Dependence of four individual LPD coefficients on current at 25°C. Total K is also shown for comparison. Vertical dotted lines mark the region where K is relatively small.

The net effect is a nearly constant K in this region, implying a linear increase of P_{LPD} with current [Eq. (2)]. Beyond the second dotted line, the coefficient representing carrier leakage increases, causing an increase of K and a corresponding super-linear increase of P_{LPD} with increasing bias current. This is due to a rapid reduction of η_i at high bias currents [Fig. 5(a)] corresponding to an internal device temperature increase in excess of 70°C [Fig. 4(b)]. Furthermore, the coefficient representing internal optical loss saturates at the thermal rollover current, which is consistent with the saturation of the photon density in the laser cavity.

This analysis suggests that, for our particular device, carrier leakage and internal optical absorption are the dominant factors among all the contributions to linear power dissipation. It also suggests that a rapid reduction of internal quantum efficiency at high bias currents and ambient temperatures, causing a rapid increase in P_{leak}, is the dominant contributor to the thermal rollover.

5. Thermal Analysis

In this section, we quantify the contributions from all heat sources (linear and quadratic) to the total heat load and to the increase of device temperature with current. Figure 6(a) shows the individual contributions of P_{LPD} and P_{QPD} to P_{tot} at $T_a = 25$, 55, and 85°C. At any T_a, P_{LPD} exceeds P_{QPD}. This may seem counterintuitive. However, the proportionality constants (R_s and K, respectively) in Eqs. (1) and (2) themselves depend on temperature, and therefore on I_b, as seen in the inset of Figs. 3(b) and 5(c), respectively. Further, with increasing T_a, P_{QPD} is slightly reduced while P_{LPD} increases progressively at any bias current.

The individual contributions of P_{leak}, P_{therm}, P_{rec}, and P_{abs} to P_{LPD} as a function of I_b are shown in Fig. 6(b) at $T_a = 25$, 55, and 85°C. At a low ambient temperature (25°C), internal optical loss (optical absorption) and carrier leakage are the two dominant power dissipation mechanisms.

#147763 - $15.00 USD Received 23 May 2011; revised 4 Jul 2011; accepted 11 Jul 2011; published 28 Jul 2011

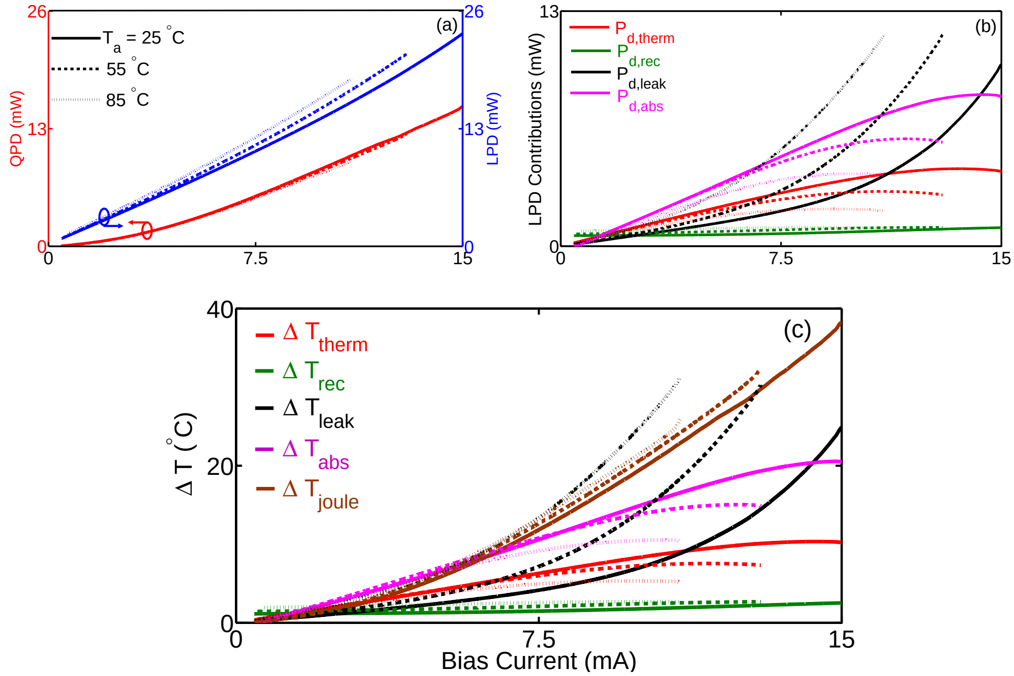

Fig. 6. Comparison of the various VCSEL heating mechanisms at three ambient temperatures. (a) Total LPD and QPD as a function of I_b; (b) dependence of individual LPD contributions on I_b, and (c) contributions of LPD and QPD mechanisms to the increase in device temperature as a function I_b.

With increasing I_b, power dissipation due to optical absorption saturates and eventually rolls over, whereas power dissipation due to carrier leakage is enhanced significantly. The rollover of the absorption heating is consistent with the rollover of the photon density while the significant increase of the leakage heating is consistent with the rapid reduction of the internal quantum efficiency at high temperatures. The reduction in η_i also causes a saturation and subsequent rollover of the power dissipation due to carrier thermalization. Finally, the slight increase of recombination heating with I_b is consistent with the increase of I_{th}, and therefore of the carrier density in the quantum wells, with increasing I_b. However, its overall contribution is negligible at any T_a and I_b. This analysis points to carrier leakage (reduction of η_i with increasing device temperature) as being the single most dominant contributor to P_{LPD} limiting the VCSEL thermal performance, especially at high ambient temperatures.

Figure 6(c) displays the contributions to current-induced self-heating as a function of I_b at $T_a = 25$, 55, and 85°C. At a low T_a of 25°C, temperature increase due to P_{QPD} (Joule heating) exceeds that due to heating from optical absorption and carrier leakage. However, at high ambient temperatures (85°C), increase in device temperature due to carrier leakage exceeds that due to other mechanisms. Also, at any T_a, heating due to carrier leakage increases most rapidly at high bias currents. This again shows that the reduction of internal quantum efficiency with increasing device temperature sets the ultimate limit for the thermal performance of this device.

Based on the preceding analysis, we draw the following conclusions regarding design modifications for improving thermal performance of VCSELs. First, to delay the onset of carrier leakage, P_{QPD} and P_{abs} must be minimized. In a conventional VCSEL with current injection through doped DBRs, this involves a trade-off since higher doping levels lead to reduced re-

#147763 - $15.00 USD Received 23 May 2011; revised 4 Jul 2011; accepted 11 Jul 2011; published 28 Jul 2011

sistance and increased free-carrier absorption [14, 25, 32]. More effective is the use of an intra-cavity contact and a dielectric top DBR [4] as both resistance and optical absorption can be reduced. In addition, it has been shown that reducing the photon lifetime through increased transmission through the top DBR can reduce internal optical absorption, thereby delaying thermal rollover [8, 21] and improving dynamic performance [10]. Second, the thermal impedance should be reduced, thereby reducing the increase of device temperature for a given amount of dissipated power. This involves the use of mounting and packaging techniques for improving thermal management and the use of more novel techniques such as integration of on-chip metallic heat spreaders [11]. Finally, further improvements are expected with active region designs that prevent an excessive increase of carrier leakage at high temperatures. This involves the design of quantum wells and barriers as well as the design of the surrounding separate confinement hetero-structure [3, 10, 31]. It may also involve the use of e.g. carrier blocking layers [26, 33].

6. Concluding Remarks

In this paper, we have presented a simple, empirical thermal model to study relative roles of various thermal rollover mechanisms inside VCSELs. The parameters required by this model are deduced experimentally through measurements of output power, voltage and emission wavelength as a function of current at different ambient temperatures, The method is quite general and can potentially be applied to any VCSEL. Specifically, we used the method for analyzing the thermal performance of an oxide-confined, 850-nm VCSEL designed with a 9-μm inner aperture diameter and optimized for high-speed operation. The model shows that the thermal saturation behavior is caused by a rapid increase of device temperature with bias current, which causes a reduction in the internal quantum efficiency, an increase in the threshold current and increase in the internal optical loss.

We carried out an in-depth analysis of various thermal rollover mechanisms for this device from the standpoint of understanding the power-saturation behavior. Our approach relates macroscopic VCSEL parameters to various thermal rollover mechanisms and makes an accurate estimate, both qualitatively and quantitatively, of various power dissipation mechanisms from the total power-dissipation in the device. We conclude that, at any bias current and ambient temperature, power dissipation due to carrier leakage, carrier thermalization, spontaneous carrier recombination and internal optical absorption together exceeds the power dissipated across the series resistance (Joule heating). This may seem counterintuitive given the fact that the basic dependence of Joule heating on current is quadratic while that of other heat sources is linear. However, the constants of proportionality (R_s and K, respectively) depend themselves on the internal device temperature, and change in opposite directions as the bias current is increased close to thermal rollover. Still, quadratic power dissipation is a major source of device heating, having a significant impact on the thermal performance of the VCSEL.

A careful analysis of the interplay among various thermal rollover mechanisms yields useful conclusions from the standpoint of improving the device design for improved thermal performance. Even though carrier leakage sets the ultimate limit for the thermal performance of our device, directly addressing it by only improving the internal quantum efficiency at high temperature is less advantageous as opposed to delaying the onset of its reduction. This can be achieved by reducing the series resistance, reducing the internal optical loss and reducing the thermal impedance, which leads to reduction of the rate of increase of device temperature with bias current. Further modifying the active region design for improved internal quantum efficiency at high temperatures may lead to a VCSEL design with superior performance in terms of both increased output optical power and speed at elevated temperatures.

#147763 - $15.00 USD Received 23 May 2011; revised 4 Jul 2011; accepted 11 Jul 2011; published 28 Jul 2011

Acknowledgments

We acknowledge financial support from the Swedish Institute Guest Scholarship, Swedish Foundation for Strategic Research (SSF), the Swedish Research Council (VR), and the European Union through the project VISIT (FP7-224211). The U.S. authors also acknowledge partial support through the National Science Foundation award ECCS-1041982. P. P. Baveja thanks Erik Haglund and Manish Jain for their useful comments on this work.